INORGANIC CHEMISTRY FRONTIERS

RESEARCH ARTICLE

View Article Online
View Journal | View Issue

Cite this: *Inorg. Chem. Front.*, 2024, **11**, 7364

Computer-aided screening of bismuth molybdates nonlinear optical crystals γ-Bi_2MoO_6†

Xuefan Wang, Yan Xiao, Wenjing Tan, Hongbo Huang, Daqing Yang, Ying Wang and Bingbing Zhang *

Received 16th July 2024,
Accepted 5th September 2024

DOI: 10.1039/d4qi01781a

rsc.li/frontiers-inorganic

Nonlinear optical (NLO) materials are key components of laser systems that extend their frequency and module laser beam. In this case, d^0 transition metals (d^0-TMs) and cations with stereochemically active lone pairs (SCALPs) can induce asymmetric coordination environment in crystals owing to second-order Jahn–Teller (SOJT) effects and accordingly are beneficial in enhancing NLO properties. In this work, the first-principles screening method was used to search for NLO materials in a bismuth molybdate system. Finally, γ-Bi_2MoO_6 and $Bi_{10}Mo_3O_{24}$ were screened and synthesized *via* high-temperature solid-state synthesis. γ-Bi_2MoO_6 showed a strong second harmonic generation (SHG) response (9.9 × KDP), large birefringence (0.21 at 1064 nm), and appropriate band gap (2.57 eV). This work presents systematic research on the application of bismuth molybdate systems as nonlinear optical materials and provides a reference for their further development.

Introduction

Nonlinear optical (NLO) crystals, which are the crucial and essential components of laser systems that widely used in laser science, signal processing, and optical communication, have attracted particular research attention.[1–3] Since the discovery of the second harmonic generation (SHG) effect, research on nonlinear optical materials has advanced significantly.[4,5] The exploration of IR NLO materials in the past decades has been extended from chalcogenides[6–9] and pnictides[10,11] to halides,[12,13] oxyhalides,[4,14,15] and transition-metal oxides.[16–19] Among them, chalcogenides and phosphides usually have some inherent drawbacks that limit their applications. For instance, the commercially available IR NLO material $AgGaS_2$ has a low laser damage threshold (LDT), while $ZnGeP_2$ suffers from two-photon absorption.[20–22] Alternatively, because of their ability to achieve equilibrated performances and grow in an open system, oxides have become promising candidates as mid-infrared NLO materials. Hence, it is urgent to explore new oxide infrared nonlinear optical materials with excellent comprehensive properties.

d^0 transition metals (Ti^{4+}, Mo^{6+}, W^{6+}, Nb^{5+}, *etc.*) and cations with stereochemically active lone pairs (SCALPs) (I^{5+}, Pb^{2+}, Te^{4+}, Bi^{3+}, *etc.*) exhibiting the second-order Jahn–Teller (SOJT) effect play an important role in the design and synthesis of NLO compounds with significant application value.[23–25] Moreover, some studies have indicated that the combination of various NLO-active units in the same compound is a successful strategy for designing promising nonlinear optical materials with enhanced SHG responses, such as $K_3V_2O_3F_4(IO_3)_3$ (1.3 × KTP at 2050 nm),[26] $Pb_2Bi(SeO_3)_2Cl_3$ (13.5 × KDP at 1064 nm),[27] $CdTeMoO_6$ (2 × KTP at 1064 nm),[28] $Cs_2TeW_3O_{12}$ (1.5 × KTP at 1064 nm),[29] and $BaNbO(IO_3)_5$ (660 × α-SiO_2 at 1064 nm).[30] Molybdates have rich chemical compositions and crystal structure types, including motifs such as [MoO_4], [MoO_5] and [MoO_6], which have been widely investigated by researchers. In addition, the magnitude of the SOJT distortion of SHG-active d^0 cations follows the following order: $Mo^{6+} > V^{5+} > W^{6+} > Ti^{4+} > Nb^{5+} > Ta^{5+} > Zr^{4+}$.[31] It is anticipated that introducing Mo^{6+} cations into a material will increase the chance of realizing an amplified SHG response. Alternatively, introducing cations with lone pair electrons in materials can enhance their birefringence and SHG performances, such as $Pb_2(NO_3)_2(H_2O)F_2$ (12 × KDP at 1064 nm),[32] $Pb_2(BO_3)(NO_3)$ (9 × KDP at 1064 nm),[33] Sn_2PO_4X (X = Br and I) (0.336–0.664 at 546 nm),[34] $Sn_9O_4Br_9X$ (X = Cl and Br) (0.273–0.258 at 1064 nm),[35] and $CsSn_2(HPO_3)_2I$ (0.200 at 546 nm).[36] Bi^{3+} cations with lone pair electrons can generate large polarizability, resulting in enhanced SHG responses, for example,

College of Chemistry and Materials Science, Institute of Life Science and Green Development, Key Laboratory of Medicinal Chemistry and Molecular Diagnosis of the Ministry of Education, State Key Laboratory of New Pharmaceutical Preparations and Excipients, Hebei University, Baoding 071002, China. E-mail: zhangbb@hbu.edu.cn

†Electronic supplementary information (ESI) available: Screening results. Calculation of dipole moments in γ-Bi_2MoO_6 and $Bi_{10}Mo_3O_{24}$. Crystal structure of $Bi_{10}Mo_3O_{24}$. Atomic coordination environment, TG-DSC analysis of γ-Bi_2MoO_6 and $Bi_{10}Mo_3O_{24}$. The PXRD of γ-Bi_2MoO_6 and $Bi_{10}Mo_3O_{24}$ samples at different calcination temperatures. The infrared vibration mode of γ-Bi_2MoO_6 and $Bi_{10}Mo_3O_{24}$. The PDOS, ELF, and SHG density maps of $Bi_{10}Mo_3O_{24}$. See DOI: https://doi.org/10.1039/d4qi01781a

$Cs_2Bi_2OSi_2O_7$ (3.5 × KDP at 1064 nm),[37] $Cd_4BiO(BO_3)_3$ (6 × KDP at 1064 nm),[38] $Bi_{32}Cd_3P_{10}O_{76}$ (4 × KDP at 1064 nm),[39] and β-$Li_2RbBi(PO_4)_2$ (5.2 × KDP at 1064 nm).[40] Considering this, we focused on bismuth molybdates, in which the d^0 transition metal Mo^{6+} and SCALP cation Bi^{3+} are combined. Bismuth molybdates are considered of great interest, which possess rich structural diversity and promising functional properties for application in catalysis, optical materials, nanoelectronics and nanophotonics.[41–43] For example, α-$Bi_2Mo_3O_{12}$, β-$Bi_2Mo_2O_9$, and γ-Bi_2MoO_6 are known for their high photoelectrochemical and photo-catalytic activities.[44] However, there are only few studies in the nonlinear optical regime, and thus further exploration is needed.

In this work, the first-principles screening method for NLO materials was used to screen bismuth molybdate NLO materials from the Inorganic Crystal Structure Database (ICSD).[45] Finally, γ-Bi_2MoO_6 and $Bi_{10}Mo_3O_{24}$ were synthesized *via* the traditional high-temperature solid-state method and their nonlinear optical properties reported. The two materials γ-Bi_2MoO_6 and $Bi_{10}Mo_3O_{24}$ exhibit significant SHG responses, which are 9.9- and 3.7-times that of KDP, respectively. Additionally, they possess appropriate band gaps of 2.57 eV and 3.02 eV, respectively. Here, we provide an in-depth examination of these target compounds, including their synthesis, thermal properties, spectroscopic characteristics, optical birefringence, and structure–property relationships.

Experimental section

Reagents

Bi_2O_3 (AR, 99.9%) and MoO_3 (AR, 99.9%) were commercially purchased and used as received without further purification.

Synthesis

Polycrystalline γ-Bi_2MoO_6 and $Bi_{10}Mo_3O_{24}$ were synthesized *via* the traditional high-temperature solid-state method. In the case of γ-Bi_2MoO_6, commercially available Bi_2O_3 and MoO_3 were completely ground in stoichiometric ratios (1 : 1) until uniformly mixed. This mixture was placed in a lidded alumina crucible and heated in the air according to the following procedure: heated to 500 °C for 8 h, held at this temperature for 24 h, and cooled to room temperature for 12 h. Then it was ground and pressed into sheets and heated to 600 °C at a rate of 1 °C min^{-1}, kept at this temperature for 6 days, and finally cooled to room temperature in 24 h. A yellow polycrystalline sample was obtained. Using the same procedure, $Bi_{10}Mo_3O_{24}$ was obtained at 750 °C in stoichiometric ratios.

Powder X-ray diffraction

The powder X-ray diffraction (PXRD) data of γ-Bi_2MoO_6 and $Bi_{10}Mo_3O_{24}$ were measured using a Bruker D8 ADVANCE X-ray diffractometer (Cu Kα, λ = 1.541 Å). The test was performed at room temperature in the 2θ range of 10–70°, with a step of 0.02° and sampling time of 2 s.

Thermal analysis

Thermal gravimetric (TG) analysis and differential scanning calorimetry (DSC) were performed on a NETZSCH STA 449C thermal analyzer instrument. The polycrystalline sample was weighed and placed in an alumina crucible, which was heated in the range of 25 °C to about 1000 °C at a rate of 10 °C min^{-1} in an air atmosphere.

Fourier transform infrared (FTIR) spectroscopy

A Nicolet IS 10 FTIR spectrometer was used to collect data in the range of 400–4000 cm^{-1} at room temperature. Using KBr as the background, a mixture of KBr and sample was pressed into a pellet for testing.

UV-vis diffuse reflectance spectroscopy

UV-vis diffuse reflectance spectra were recorded using a Shimadzu UV-3600 spectrometer in the range of 300 to 800 nm at room temperature.

SHG measurement

The powder SHG effect of the γ-Bi_2MoO_6 and $Bi_{10}Mo_3O_{24}$ crystals were tested using the Kurtz and Perry method[46] and an Nd:YAG Q-modulated laser with a wavelength of 1064 nm and a KDP crystal as a reference. The γ-Bi_2MoO_6 and $Bi_{10}Mo_3O_{24}$ samples and the KDP reference sample were ground into different particle sizes, and then screened, and the powders were sieved into several different particle size ranges of 20–38.5, 38.5–55, 55–88, 88–125, 125–160, 160–200 and 200–250 μm.

Theoretical calculation

The electronic structure of γ-Bi_2MoO_6 and $Bi_{10}Mo_3O_{24}$ was investigated using first-principle calculations performed using the CASTEP package based on density functional theory (DFT).[47] The Perdew–Burke–Ernzerhof (PBE) generalized gradient approximation (GGA) functional for electron exchange-related energies and the norm-conserving pseudopotential to describe electron-nucleus interactions were adopted.[48] The γ-Bi_2MoO_6 and $Bi_{10}Mo_3O_{24}$ structures were used for theoretical calculations and tested for convergence with the plane-wave energy cutoff and interatomic force of 750 eV and 1×10^{-6} eV A^{-1}, respectively. The Monkhorst–Pack method was used for the integration of the Brillouin zone for the selection of *k*-space grid points, and the final *k*-points were set to 5 × 2 × 5 and 1 × 4 × 3, respectively.

Results and discussion

We focused on the bismuth molybdate system and 5 asymmetric structures containing Bi, Mo and O elements were searched from the Inorganic Crystal Structure Database (ICSD). Then, the band gap, birefringence, and second-order susceptibility $\chi^{(2)}$ of these bismuth molybdates were successfully calculated using the DFT method (Table S1†). Molybdate possesses a wide transmission window in the infrared region,

and accordingly can be used as a mid-infrared NLO material. We expected to obtain materials with a large SHG response ($\chi^{(2)} > 7.8$ pm V^{-1}). Finally, the γ-Bi_2MoO_6 and $Bi_{10}Mo_3O_{24}$ compounds were successfully synthesized.

The structure of γ-Bi_2MoO_6 was first reported by Van den Elzen and Rieck in 1973.[49] In 1986, VK Yanovskii reported that its SHG intensity reached 60 to 80 in units of $I_{2\omega}$ of quartz but did not further explore its NLO-related properties.[50] Herein, low-temperature phase γ-Bi_2MoO_6 was synthesized, belonging to the $Pca2_1$ (no. 29) space group with cell parameters a = 5.487(2) Å, b = 16.226(6) Å, c = 5.506(2) Å, and Z = 4. Its asymmetric unit contains two Bi atoms, one Mo atom, and six O atoms. In this structure, each Mo atom is coordinated with six O atoms to form an MoO_6 octahedron. A significant distortion towards the edge (C_2, Δd = 1.64) was observed in the MoO_6 octahedron,[51] which is highly beneficial in achieving a large local microscopic polarizability and leads to an enhanced SHG response. The MoO_6 octahedra are interconnected by co-angled O atoms, which share angles along the a and c directions to form an infinite $[MoO_4]^{2-}$ layer (Fig. 1b). The $[Bi_2O_2]^{2+}$ layer consists of a square planar network of O^{2-} anions (Fig. 1c), with Bi^{3+} cations alternating above and below the planes, which can be described as forming a BiO_4 square pyramidal cap. Besides, each Bi atoms are connected with two vertex O atoms of MoO_6 octahedra to form BiO_6 polyhedron with stereochemically active construction. The $[Bi_2O_4]^{2-}$ and $[MoO_4]^{2-}$ layers are alternately stacked along the b-axis by sharing vertex O atoms to form the three-dimensional crystal structure of γ-Bi_2MoO_6 (Fig. 1a).

$Bi_{10}Mo_3O_{24}$ crystallizes in the monoclinic crystal system noncentrosymmetric space group $C2$ (no. 5) with the cell parameters of a = 23.72316(5) Å, b = 5.64745(1) Å, c = 8.68034(2) Å, β = 95.8734(1)°, and Z = 2. The asymmetric unit of $Bi_{10}Mo_3O_{24}$ consists of five Bi, two Mo and thirteen O, which are crystallographically independent atoms. The structure of $Bi_{10}Mo_3O_{24}$, as projected onto the ac plane, is depicted in Fig. S4c.† Its overall structure is composed of an infinite $[Bi_{10}O_{12}]_n$ layer (Fig. S4a†), which is oriented parallel to the b direction and repetitively arranged along the c direction. The Bi^{3+} cations within the $[Bi_{10}O_{12}]_n$ layers are coordinated with four, five and six O atoms, forming the BiO_n (n = 4, 5, 6) polyhedra with Bi–O bond lengths in the range of 2.023 to 2.692 Å. The $\{3[MoO_4]^{2-}\}_m$ tetrahedral groups are situated within the ten-membered ring channels composed of bismuth polyhedra and balance the charge of the structure (Fig. S4b†).

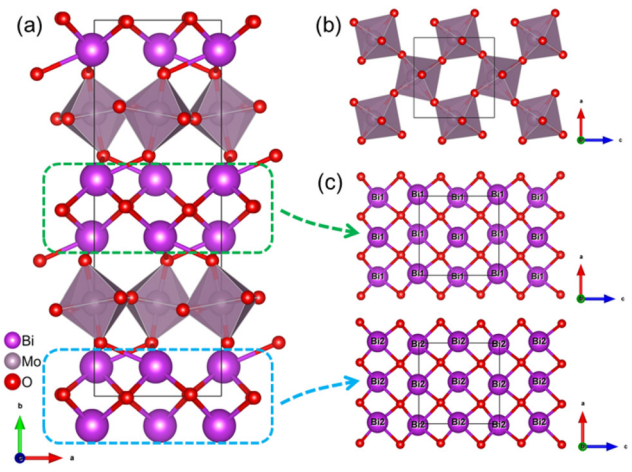

Fig. 1 Schematic crystal structure of γ-Bi_2MoO_6 (a), MoO_6 octahedron (b) and $[Bi_2O_2]^{2+}$ layer (c).

To study the relationship between macroscopic symmetry and microstructure, the local dipole moments of the polyhedra within the crystal structure and the net dipole moment within the unit cell were calculated using the bond-valence method (Tables S2 and S3†). In γ-Bi_2MoO_6 and $Bi_{10}Mo_3O_{24}$, the Bi–O polyhedra are severely distorted and exhibit significant dipole moments (γ-Bi_2MoO_6: 15.061–17.406 D; $Bi_{10}Mo_3O_{24}$: 14.861–19.929 D), which may be ascribed to the SCALP of electrons in the Bi^{3+} cation. Due to the influence of the SOJT effect, the Mo–O polyhedra also undergo varying degrees of distortion. In the case of γ-Bi_2MoO_6, as a result of its crystal symmetry, the local dipole moments add up and the a and b components of the net dipole moment within the unit cell are canceled, leading to macroscopic polarization along the c-axis. Similarly, $Bi_{10}Mo_3O_{24}$ exhibits a net dipole moment directed along the b-axis. The total dipole moment along the c-axis for γ-Bi_2MoO_6 is 19.813 D, with a dipole moment density of 0.040 D Å^{-3}. Along the b-axis for $Bi_{10}Mo_3O_{24}$, the total dipole moment is 35.594 D, and the dipole moment density was calculated to be 0.031 D Å^{-3}. The large dipole moments of Bi–O polyhedra indicate strong distortion resulting from SCALP. These two compounds, with their large net dipole moments, are instrumental in achieving optical anisotropy and NLO performance.

The γ-Bi_2MoO_6 and $Bi_{10}Mo_3O_{24}$ polycrystals were synthesized *via* the high-temperature solid-phase method. As shown in Fig. 2a and b, the experimental and calculated values in the PXRD plot are consistent, which demonstrates the high purity of γ-Bi_2MoO_6 and $Bi_{10}Mo_3O_{24}$, respectively. The thermal characteristics were evaluated through TG/DSC examinations. The TG curves of γ-Bi_2MoO_6 and $Bi_{10}Mo_3O_{24}$ showed no significant weight loss between room temperature and about 1000 °C (Fig. S6a and S6b,† respectively). In the DSC curves (Fig. S6a†), γ-Bi_2MoO_6 has a phase transition at 641.7 °C.[52] Combined with the PXRD patterns of the γ-Bi_2MoO_6 samples heated at different temperature (Fig. S6c†), the transferred phase is γ'-Bi_2MoO_6 that crystallized in the space group of $P2_1/c$. The new phase melts at 929.2 °C and decomposes at 966.5 °C. As show in Fig. S6c,† some minor impurity peaks were detected at 950 °C and the peaks became obvious at 1000 °C, proving that γ'-Bi_2MoO_6 will decompose at high temperatures. The DSC profile and PXRD pattern (Fig. S6b and S6d,† respectively) indicate that $Bi_{10}Mo_3O_{24}$ undergoes decomposition at 864.2 °C to form a mixture of $Bi_{38}Mo_7O_{78}$ oxide and unknown high-temperature solid solution,[53] and subsequently melted at 946.5 °C. The thermal behaviors of the two crystals suggest that the low temperature flux method is needed to grow single crystals.

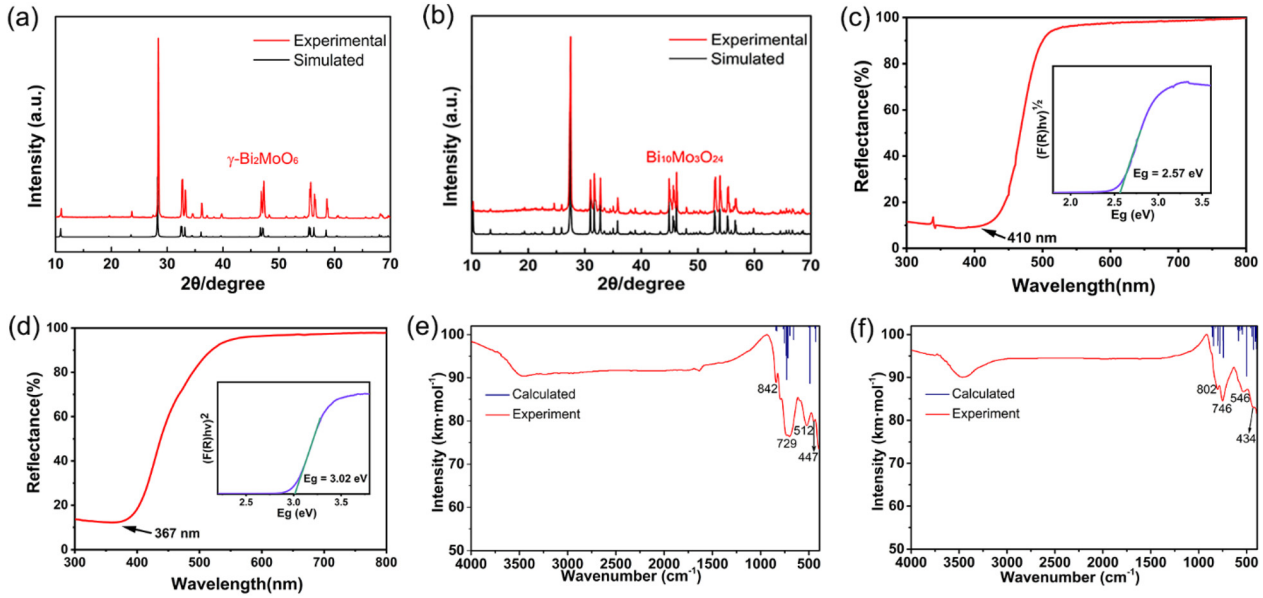

Fig. 2 Powder X-ray diffraction patterns of γ-Bi_2MoO_6 (a) and $Bi_{10}Mo_3O_{24}$ (b). UV-vis diffuse reflectance spectra of γ-Bi_2MoO_6 (c) and $Bi_{10}Mo_3O_{24}$ (d). FT-IR spectra of γ-Bi_2MoO_6 (e) and $Bi_{10}Mo_3O_{24}$ (f) samples.

The data collected by UV-Vis diffuse reflectance spectroscopy were processed using the Tauc plot method,[54] and it was found that γ-Bi_2MoO_6 shows a band gap of 2.57 eV, which is consistent with the yellow color exhibited by its crystal. Its UV cut-off edge is about 410 nm (Fig. 2c). Furthermore, the UV cut-off edge of $Bi_{10}Mo_3O_{24}$ is 367 nm. The experimental band gap is 3.02 eV (Fig. 2d). The values of these two compounds are comparable to that of molybdates, such as $CeClMoO_4$ (2.91 eV),[55] $CeBrMoO_4$ (2.81 eV),[55] and MoO_2Cl_2 (2.88 eV).[56]

The infrared spectra show absorption bands between 400 and 4000 cm^{-1}, which were employed to elucidate the IR absorption models. In the case of γ-Bi_2MoO_6 (Fig. 2e), with the absorption peak of the stretching vibration of the Bi–O bond located near 447 cm^{-1} and the absorption band of the Mo–O–Bi vibration mode near 510 cm^{-1}.[57] The absorption peaks at 729 and 842 cm^{-1} represent the Mo–O stretching vibration.[58] In the case of $Bi_{10}Mo_3O_{24}$ (Fig. 2f), the peaks at about 434 and 546 cm^{-1} can be ascribed to the Bi–O bond vibrations, while the bands at 746 and 802 cm^{-1} are ascribed to the Mo–O tetrahedral stretching vibration. Using density functional theory calculations, we simulated the infrared vibration modes of γ-Bi_2MoO_6 (Fig. S7†) and $Bi_{10}Mo_3O_{24}$ (Fig. S8†). The experimental results are consistent with the simulated spectrum. The IR absorption spectra indicate that two compounds have no intrinsic absorption in a broad transmission range.

The SHG responses of the sieved γ-Bi_2MoO_6 and $Bi_{10}Mo_3O_{24}$ samples with different particle sizes were measured using the Kurtz-Perry method at room temperature with a laser beam with a wavelength of 1064 nm from an Nd:YAG laser. As shown in Fig. 3, the powder SHG intensity of the two samples increased with an increase in their particle size, which indicates that it can achieve phase matching. γ-Bi_2MoO_6 and $Bi_{10}Mo_3O_{24}$ exhibited SHG responses of 9.9- and 3.7-times that of the KDP samples, respectively, when measured with a particle size in the range of 200–250 μm. To evaluate the performance of γ-Bi_2MoO_6 and $Bi_{10}Mo_3O_{24}$, the SHG effect of pure molybdate NLO materials were surveyed, as shown in Table 1. It can be seen that γ-Bi_2MoO_6 has an excellent SHG performance, which indicates that γ-Bi_2MoO_6 is a promising IR NLO crystal material. Restricted by Kleinman symmetry, three (d_{15}, d_{24}, and d_{33}) and four (d_{16}, d_{14}, d_{22}, and d_{23}) independent nonzero SHG tensors for γ-Bi_2MoO_6 and $Bi_{10}Mo_3O_{24}$ should be considered, respectively. To get accurate calculation results, we set the scissors operator value as 1.58 eV for γ-Bi_2MoO_6 and

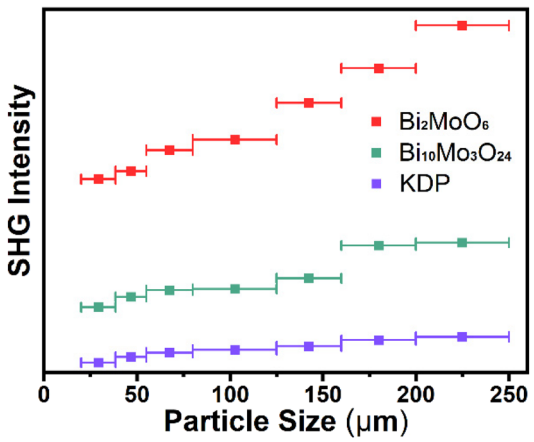

Fig. 3 SHG intensities *vs.* particle sizes with a 1064 nm pump for γ-Bi_2MoO_6 and $Bi_{10}Mo_3O_{24}$ compared with benchmark KDP with the same particle size.

Table 1 Comparison of the SHG effect of typical molybdate NLO materials

No.	Material	Space group	SHG	Ref.
1	$Cs_2NaBi(MoO_4)_3$	*R*3*c*	5 × α-SiO_2[b]	59
2	$LiNa_5Mo_9O_{30}$	*Fdd*2	2 × KDP[b]	60
3	$LaBrMoO_4$	*Pc*	0.47 × KDP[b]	61
4	$Ba_2MoO_3F_4$	*Cc*	8 × α-SiO_2[b]	62
5	β-$BaMo_3O_{10}$	$P2_1$	1.2 × KDP[b]	63
6	α-$BaMoO_2F_4$	$Pca2_1$	0.7 × α-SiO_2[b]	64
7	$SrMoO_2F_4$	$Pca2_1$	1.1 × α-SiO_2[b]	64
8	$PbMoO_2F_4$	$Pca2_1$	0.5 × α-SiO_2[b]	64
9	$KMoO_2F_3$	$P2_12_12_1$	0.4 × α-SiO_2[b] (NPM)	65
10	$(Ag_3MoO_3F_3)(Ag_3MoO_4)Cl$	*P*3*m*1	10 × α-SiO_2[b]	66
11	$K_{10}(Mo_2O_4F_7)_3Cl$	$Pmn2_1$	0.8 × KDP[b] (NPM)	67
12	$K_7Ag(MoO_4)_4$	$P6_3mc$	2.9 × α-SiO_2[b]	68
13	$CeClMoO_4$	*Pc*	0.06 × AGS[c]	55
14	$CeBrMoO_4$	*Pc*	0.58 × AGS[c]	55
15	MoO_2Cl_2	*Fmm*2	2.1 × KTP[c]	56
16	$Bi_{10}Mo_3O_{24}$[a]	*C*2	3.7 × KDP[b]	This work
17	γ-Bi_2MoO_6[a]	$Pca2_1$	9.9 × KDP[b]	This work

[a] This work. [b] The SHG efficiency at 1064 nm. [c] The SHG efficiency at around 2090 nm.

0.51 eV for $Bi_{10}Mo_3O_{24}$. The calculated SHG coefficients of γ-Bi_2MoO_6 are d_{15} = −6.78, d_{24} = 12.78 and d_{33} = 5.80 pm V^{-1}, while the SHG coefficients of d_{16}, d_{14}, d_{22}, and d_{23} for $Bi_{10}Mo_3O_{24}$ are −1.71, 2.54, 1.67, and −0.30 pm V^{-1}, respectively.

The nonlinear optical properties were further investigated by theoretical means to reveal the origin of the SHG response. The calculated electronic band structure indicated that γ-Bi_2MoO_6 has an indirect band gap of 0.99 eV (Fig. 4a), and $Bi_{10}Mo_3O_{24}$ has a direct band gap of 2.51 eV (Fig. 4b). Due to the discontinuity of the exchange–correlation energy functional, the band gaps are underestimated. Thus, to obtain the accurate band gap of γ-Bi_2MoO_6, the HSE06 hybrid exchange–correlation functional was used, and its band gap was calculated to be 1.97 eV (Fig. S9†), which is very close to its experimental band gap. The refractive index dispersion curves of the γ-Bi_2MoO_6 and $Bi_{10}Mo_3O_{24}$ compounds were also calculated. Based on the refractive index curve with the scissors operator, the birefringence at 1064 nm (Δn_{cal}) was calculated to be 0.21 and 0.03 (Fig. 4c and d), respectively.

According to the calculated partial densities of states (PDOS), it can be seen that γ-Bi_2MoO_6 and $Bi_{10}Mo_3O_{24}$ exhibit similar electronic structures. The O 2p states and less Bi 6s6p were located in the top of the valence band (TVB) (−5–0 eV), and the bottom of the conduction band (BCB) (0–5 eV) is mainly occupied by the O 2p and Mo 4d states (Fig. 4a and b). Theoretical studies have shown that nonlinear optical properties are directly related to the leap between the states of electrons near the Fermi energy level. Therefore, the optical properties of γ-Bi_2MoO_6 and $Bi_{10}Mo_3O_{24}$ were determined based on the synergistic effect of the O-2p and Bi 6s6p orbitals in the occupied states, while the Mo-4d and O-2p orbitals in Mo–O polyhedra in the unoccupied states. To further study the stereoactivity of the lone pair electrons on the Bi^{3+} cations located in different environments, the Bi-related PDOS diagrams and the electron localization function (ELF) were calcu-

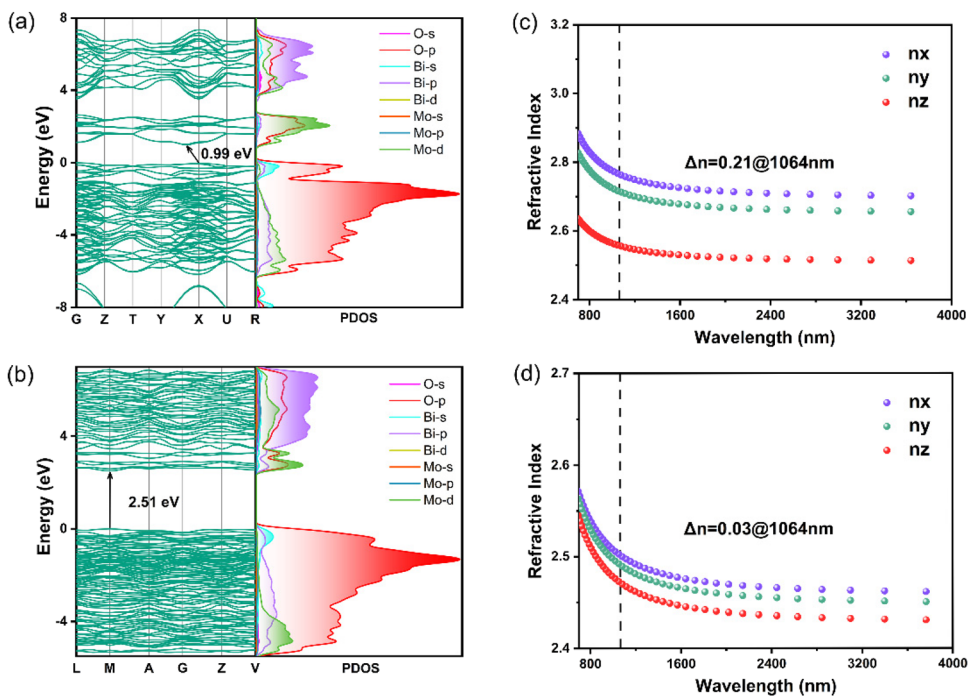

Fig. 4 Calculated band structure and partial densities of states of γ-Bi_2MoO_6 (a) and $Bi_{10}Mo_3O_{24}$ (b) and refractive index dispersion of γ-Bi_2MoO_6 (c) and $Bi_{10}Mo_3O_{24}$ (d).

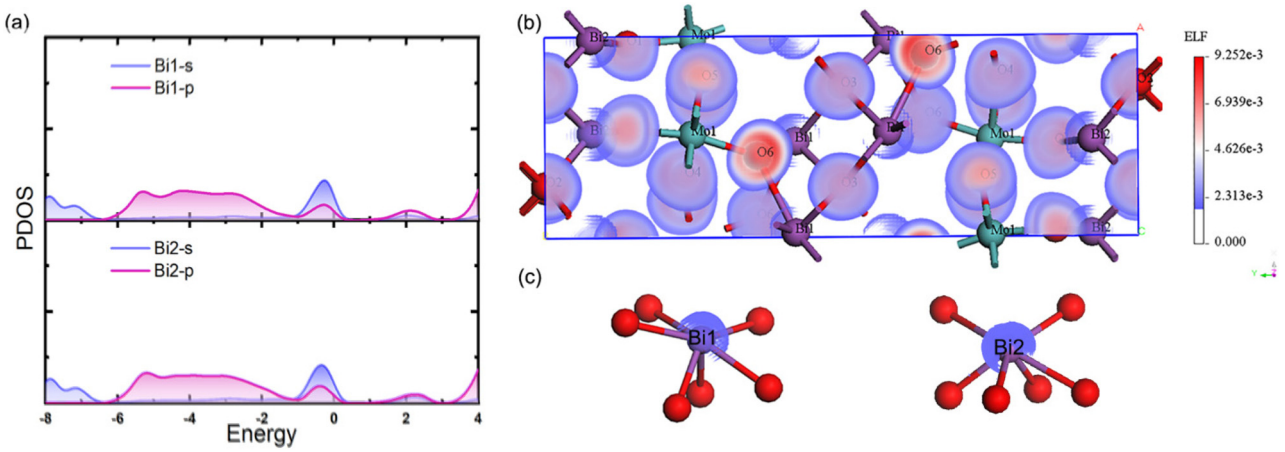

Fig. 5 Partial DOSs of Bi1 and Bi2 atoms from γ-Bi_2MoO_6 (a). ELF of γ-Bi2MoO6 (b). ELF for two independent Bi atoms in γ-Bi_2MoO_6 (c).

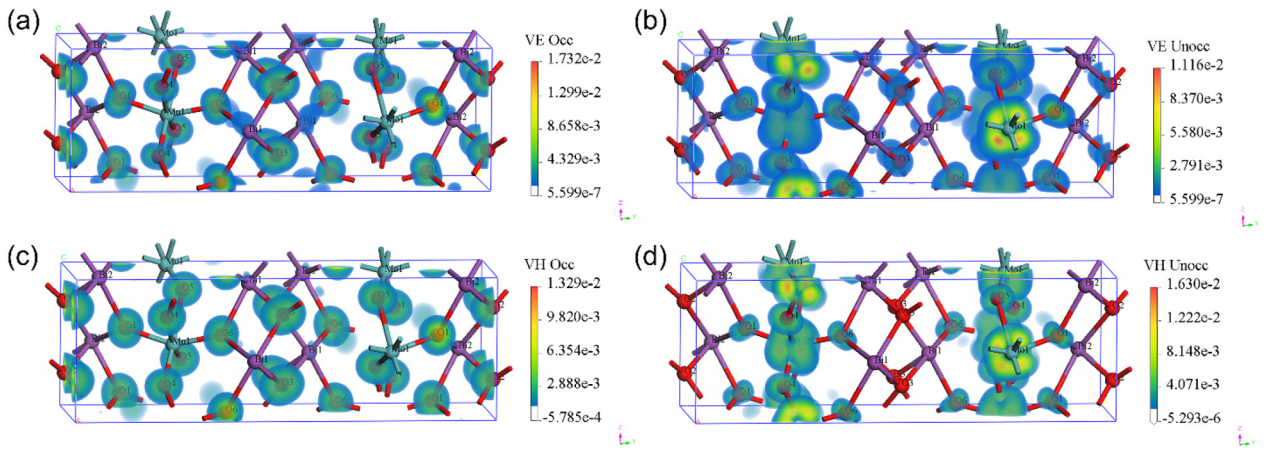

Fig. 6 SHG density maps of (a) occupied and (b) unoccupied orbitals of virtual-electron (VE) part as well as (c) occupied and (d) unoccupied orbitals of virtual-hole (VH) part of the largest SHG coefficient d_{24} for γ-Bi_2MoO_6.

lated for γ-Bi_2MoO_6. According to the PDOS diagrams (Fig. 5a), it can be seen that the 6s orbitals of each Bi atom occupy the TVB, contributing to the lone pair electronic configuration and optical properties of the materials. The two individual Bi atoms in γ-Bi_2MoO_6 exhibit hemispherical isosurfaces (Fig. 5b and c, respectively), confirming the stereoactivity of the Bi^{3+}-$6s^2$ lone pair electrons. The five individual Bi atoms in $Bi_{10}Mo_3O_{24}$ exhibit similar electronic characters to that of γ-Bi_2MoO_6, as shown in Fig. S10.†

The contributions to the SHG responses were analyzed using the SHG-weighted electron density of the largest tensor. The SHG density was plotted to show the electron orbitals that contribute to SHG in real space. In γ-Bi_2MoO_6, both the virtual-electron (VE) and virtual-hole (VH) processes contribute equally to the SHG tensor d_{24}. Additionally, the VE process has a larger contribution (91.8%) to the SHG effects in $Bi_{10}Mo_3O_{24}$ than that of the VH process. According to the SHG density diagram of the occupied orbitals in γ-Bi_2MoO_6, it can be observed that the contribution of the O2 and O3 atoms shared by Bi and Bi are higher than that of the O1 and O6 atoms shared by Bi and Mo, which are higher than that of O4 and O5 atoms shared by Mo and Mo (Fig. S11†). Besides, the lone pair electrons of Bi atom also have slight contributions to SHG. Therefore, the SHG density of γ-Bi_2MoO_6 in the occupied states mainly accumulates on the BiO_6 polyhedra, while the orbitals belonging to MoO_6 octahedra are the main source in the unoccupied states (Fig. 6). In the case $Bi_{10}Mo_3O_{24}$ (Fig. S12†), the results indicate that the BiO_n (n = 4, 5, 6) polyhedra in the occupied states and MoO_4 groups in the unoccupied states dominate the SHG contributions.

Conclusions

In summary, based on the DFT method, the first-principles screening method was used to search for exceptional nonlinear optical (NLO) materials in bismuth molybdates. Finally, two bismuth molybdates, γ-Bi_2MoO_6 and $Bi_{10}Mo_3O_{24}$, were

screened and synthesized *via* a solid-state reaction. γ-Bi_2MoO_6 exhibited a strong SHG intensity of 9.9 times that of KDP and a large birefringence of 0.21 at 1064 nm. $Bi_{10}Mo_3O_{24}$ exhibited the SHG effect of about 3.7 × KDP. The theoretical research results indicate that the SHG response of the title compound originates from the BiO_n polyhedra in the occupied states, while the MoO_n polyhedra in unoccupied states. This report on the two compounds will provide further insights for exploring nonlinear optical crystals of bismuth molybdates and obtaining excellent candidates for the next step of development.

Author contributions

The manuscript was written through the contributions of all authors. All authors have given approval to the final version of the manuscript.

Data availability

The raw data supporting the conclusions of this manuscript will be made available by the authors, without undue reservation, to any qualified researcher.

The authors confirm that the data supporting the findings of this study are available within the article and its ESI.†

Conflicts of interest

There are no conflicts to declare.

Acknowledgements

This work was supported by the National Natural Science Foundation of China (Grant No. 52072109 and 22101069); the Science and Technology Project of Hebei Education Department (Grant No. BJK2023029); the Natural Science Foundation of Hebei Province (Grant No. B2023201068); Key Laboratory of Chemical Biology of Hebei Province (22567635H); the Key Laboratory of Analytical Science and Technology of Hebei Province (No. 22567620H).

References

1 Y. Pan, S. P. Guo, B. W. Liu, H. G. Xue and G. C. Guo, Second-order nonlinear optical crystals with mixed anions, *Coord. Chem. Rev.*, 2018, **374**, 464–496.
2 H. X. Fan, N. Ye and M. Luo, New Functional Groups Design toward High Performance Ultraviolet Nonlinear Optical Materials, *Acc. Chem. Res.*, 2023, **56**, 3099–3109.
3 Z. T. Yan, J. B. Fan, S. L. Pan and M. Zhang, Recent advances in rational structure design for nonlinear optical crystals: leveraging advantageous templates, *Chem. Soc. Rev.*, 2024, **53**, 6568–6599.
4 H. Zhang, M. Zhang, S. L. Pan, X. Y. Dong, Z. H. Yang, X. L. Hou, Z. Wang, K. B. Chang and K. R. Poeppelmeier, $Pb_{17}O_8Cl_{18}$: A Promising IR Nonlinear Optical Material with Large Laser Damage Threshold Synthesized in an Open System, *J. Am. Chem. Soc.*, 2015, **137**, 8360–8363.
5 J. D. Chen, C. S. Lin, D. Zhao, M. Luo, G. Peng, B. X. Li, S. D. Yang, Y. S. Sun and N. Ye, Anionic Aliovalent Substitution from Structure Models of ZnS: Novel Defect Diamond-like Halopnictide Infrared Nonlinear Optical Materials with Wide Band Gaps and Large SHG Effects, *Angew. Chem., Int. Ed.*, 2020, **59**, 23549–23553.
6 C. X. Li, X. H. Meng, Z. Li and J. Y. Yao, Hg-based chalcogenides: An intriguing class of infrared nonlinear optical materials, *Coord. Chem. Rev.*, 2022, **453**, 214328.
7 W. F. Zhou, J. J. Wu, W. L. Liu and S. P. Guo, Ag-based chalcogenides and derivatives as promising infrared nonlinear optical materials, *Coord. Chem. Rev.*, 2023, **477**, 214950.
8 L. F. Dong, S. Z. Zhang, P. F. Gong, L. Kang and Z. S. Lin, Evaluation and prospect of Mid-Infrared nonlinear optical materials in f^0 rare earth (RE = Sc, Y, La) chalcogenides, *Coord. Chem. Rev.*, 2024, **509**, 215805.
9 K. Wu and S. L. Pan, A review on structure-performance relationship toward the optimal design of infrared nonlinear optical materials with balanced performances, *Coord. Chem. Rev.*, 2018, **377**, 191–208.
10 S. Lee, S. L. Carnahan, G. Akopov, P. Yox, L. L. Wang, A. J. Rossini, K. Wu and K. Kovnir, Noncentrosymmetric Tetrel Pnictides $RuSi_4P_4$ and $IrSi_3P_3$: Nonlinear Optical Materials with Outstanding Laser Damage Threshold, *Adv. Funct. Mater.*, 2021, **31**, 2010293.
11 J. D. Chen, Q. C. Wu, H. T. Tian, X. T. Jiang, F. Xu, X. Zhao, Z. S. Lin, M. Luo and N. Ye, Uncovering a Vital Band Gap Mechanism of Pnictides, *Adv. Sci.*, 2022, **9**, 2105787.
12 P. F. Gong, F. Liang, L. Kang, X. G. Chen, J. G. Qin, Y. C. Wu and Z. S. Lin, Recent advances and future perspectives on infrared nonlinear optical metal halides, *Coord. Chem. Rev.*, 2019, **380**, 83–102.
13 P. F. Gong, F. Liang, L. Kang and Z. S. Lin, Mid-Infrared Nonlinear Optical Halides with Diamond-like Structures: A Theoretical and Experimental Study, *Chem. Mater.*, 2022, **34**, 5301–5310.
14 X. L. Chen, H. Jo and K. M. Ok, Lead Mixed Oxyhalides Satisfying All Fundamental Requirements for High–Performance Mid–Infrared Nonlinear Optical Materials, *Angew. Chem.*, 2020, **132**, 7584–7590.
15 X. L. Chen and K. M. Ok, Metal oxyhalides: an emerging family of nonlinear optical materials, *Chem. Sci.*, 2022, **13**, 3942–3956.
16 H. C. Lan, F. Liang, X. X. Jiang, C. Zhang, H. H. Yu, Z. S. Lin, H. J. Zhang, J. Y. Wang and Y. C. Wu, Pushing Nonlinear Optical Oxides into the Mid-Infrared Spectral Region Beyond 10 μm: Design, Synthesis, and

Characterization of $La_3SnGa_5O_{14}$, *J. Am. Chem. Soc.*, 2018, **140**, 4684–4690.

17 J. B. Huang, S. R. Guo, Z. Z. Zhang, Z. H. Yang and S. L. Pan, Designing excellent mid-infrared nonlinear optical materials with fluorooxo-functional group of d^0 transition metal oxyfluorides, *Sci. China Mater.*, 2019, **62**, 1798–1806.

18 J. Yu, B. B. Zhang, X. D. Zhang, Y. Wang, K. Wu and M. H. Lee, Finding Optimal Mid-Infrared Nonlinear Optical Materials in Germanates by First-Principles High-Throughput Screening and Experimental Verification, *ACS Appl. Mater. Interfaces*, 2020, **12**, 45023–45035.

19 X. L. Du, X. J. Guo, Z. L. Gao, F. A. Liu, F. F. Guo, S. Y. Wang, H. Y. Wang, Y. X. Sun and X. T. Tao, Li_2MTeO_6 (M=Ti, Sn): Mid–Infrared Nonlinear Optical Crystal with Strong Second Harmonic Generation Response and Wide Transparency Range, *Angew. Chem., Int. Ed.*, 2021, **60**, 23320–23326.

20 K. Wu, B. B. Zhang, Z. H. Yang and S. L. Pan, New Compressed Chalcopyrite-like $Li_2BaMIVQ_4$ (MIV = Ge, Sn; Q = S, Se): Promising Infrared Nonlinear Optical Materials, *J. Am. Chem. Soc.*, 2017, **139**, 14885–14888.

21 H. Lin, W. B. Wei, H. Chen, X. T. Wu and Q. L. Zhu, Rational design of infrared nonlinear optical chalcogenides by chemical substitution, *Coord. Chem. Rev.*, 2020, **406**, 213150.

22 J. D. Chen, X. T. Jiang, Q. C. Wu, Z. S. Lin, M. Luo and N. Ye, Pnictides: An emerging class of infrared nonlinear optical material candidates, *J. Alloys Compd.*, 2022, **901**, 163384.

23 L. Kang, M. L. Zhou, J. Y. Yao, Z. S. Lin, Y. C. Wu and C. T. Chen, Metal Thiophosphates with Good Mid-infrared Nonlinear Optical Performances: A First-Principles Prediction and Analysis, *J. Am. Chem. Soc.*, 2015, **137**, 13049–13059.

24 M. J. Xia, X. X. Jiang, Z. S. Lin and R. K. Li, "All-Three-in-One": A New Bismuth–Tellurium–Borate Bi_3TeBO_9 Exhibiting Strong Second Harmonic Generation Response, *J. Am. Chem. Soc.*, 2016, **138**, 14190–14193.

25 C. Wu, G. Yang, M. G. Humphrey and C. Zhang, Recent advances in ultraviolet and deep-ultraviolet second-order nonlinear optical crystals, *Coord. Chem. Rev.*, 2018, **375**, 459–488.

26 J. Chen, C. L. Hu, Y. L. Lin, Y. Chen, Q. Q. Chen and J. G. Mao, $K_3V_2O_3F_4(IO_3)_3$: a high-performance SHG crystal containing both five and six-coordinated V^{5+} cations, *Chem. Sci.*, 2022, **13**, 454–460.

27 Y. J. Jia, X. Y. Zhang, Y. G. Chen, X. X. Jiang, J. N. Song, Z. S. Lin and X. M. Zhang, $PbBi(SeO_3)_2F$ and $Pb_2Bi(SeO_3)_2Cl_3$: Coexistence of Three Kinds of Stereochemically Active Lone-Pair Cations Exhibiting Excellent Nonlinear Optical Properties, *Inorg. Chem.*, 2022, **61**, 15368–15376.

28 S. G. Zhao, X. X. Jiang, R. He, S. Q. Zhang, Z. H. Sun, J. H. Luo, Z. S. Lin and M. C. Hong, A combination of multiple chromophores enhances second-harmonic generation in a nonpolar noncentrosymmetric oxide: $CdTeMoO_6$, *J. Mater. Chem. C*, 2013, **1**, 2906–2912.

29 P. Zhao, H. Cong, X. Tian, Y. Sun, C. Zhang, S. Xia, Z. Gao and X. Tao, Top-Seeded Solution Growth, Structure, Morphology, and Functional Properties of a New Polar Crystal —$Cs_2TeW_3O_{12}$, *Cryst. Growth Des.*, 2015, **15**, 4484–4489.

30 C. F. Sun, C. L. Hu, X. Xu, J. B. Ling, T. Hu, F. Kong, X. F. Long and J. G. Mao, $BaNbO(IO_3)_5$: a new polar material with a very large SHG response, *J. Am. Chem. Soc.*, 2009, **131**, 9486–9487.

31 K. M. Ok, P. S. Halasyamani, D. Casanova, M. Llunell, P. Alemany and S. Alvarez, Distortions in Octahedrally Coordinated d^0 Transition Metal Oxides: A Continuous Symmetry Measures Approach, *Chem. Mater.*, 2006, **18**, 3176–3183.

32 G. Peng, Y. Yang, Y. H. Tang, M. Luo, T. Yan, Y. Q. Zhou, C. S. Lin, Z. S. Lin and N. Ye, Collaborative enhancement from Pb^{2+} and F^- in $Pb_2(NO_3)_2(H_2O)F_2$ generates the largest second harmonic generation effect among nitrates, *Chem. Commun.*, 2017, **53**, 9398–9401.

33 J. L. Song, C. L. Hu, X. Xu, F. Kong and J. G. Mao, A Facile Synthetic Route to a New SHG Material with Two Types of Parallel π–Conjugated Planar Triangular Units, *Angew. Chem., Int. Ed.*, 2015, **54**, 3679–3682.

34 J. Y. Guo, A. Tudi, S. J. Han, Z. H. Yang and S. L. Pan, Sn_2PO_4I: An Excellent Birefringent Material with Giant Optical Anisotropy in Non π–Conjugated Phosphate, *Angew. Chem., Int. Ed.*, 2021, **60**, 24901–24904.

35 M. Hu, C. C. Tu, Z. H. Yang, S. J. Han and S. L. Pan, $Sn_9O_4Br_9X$ (X = Cl, Br): Two new Sn(II) oxyhalides exhibiting large birefringence derived from highly distortive polyhedra of lone pair cations, *Scr. Mater.*, 2023, **231**, 115437.

36 L. Ma, W. Xu, L. Xu, Y. L. Lv, W. Liu, S. P. Guo and R. L. Tang, $CsSn_2(HPO_3)_2I$: The first inorganic metal phosphite iodide as a promising birefringent material exhibits a large birefringence with ideally layered framework, *Scr. Mater.*, 2024, **242**, 115913.

37 W. L. Zhao, C. G. Li, T. Han, J. M. Jiao, Y. H. She, D. X. Ju, F. Liang, N. Ye, Z. G. Hu and Y. C. Wu, $Cs_2Bi_2OSi_2O_7$: A Promising Bismuth Silicate Nonlinear Optical Crystal with Face-Sharing BiO_5 Polyhedra Exhibiting Strengthened Second Harmonic Generation Response and Birefringence, *Chem. Mater.*, 2022, **34**, 3365–3372.

38 W. L. Zhang, W. D. Cheng, H. Zhang, L. Geng, C. S. Lin and Z. Z. He, A Strong Second-Harmonic Generation Material $Cd_4BiO(BO_3)_3$ Originating from 3-Chromophore Asymmetric Structures, *J. Am. Chem. Soc.*, 2010, **132**, 1508–1509.

39 J. K. Wang, B. K. Xiong, H. P. Wu, H. W. Yu, Z. G. Hu, J. Y. Wang and Y. C. Wu, $Bi_{32}Cd_3P_{10}O_{76}$: a new congruently melting nonlinear optical crystal with a large SHG response and a wide transparent region, *Inorg. Chem. Front.*, 2021, **8**, 344–351.

40 L. Wu, R. X. Zhang, Q. Jing, H. Y. Huang, X. M. He, Z. C. Wang and Z. H. Chen, Modulating optical perform-

ance by phase transition in a nonlinear optical material (-$Li_2RbBi(PO_4)_2$, *Inorg. Chem. Front.*, 2023, **10**, 4496–4502.
41 Z. S. Wang, S. L. Bi, Y. P. Wan, P. J. Huang and M. Zheng, Optical properties of a new $Bi_{38}Mo_7O_{78}$ semiconductor with fluorite-type δ-Bi_2O_3 structure, *Appl. Surf. Sci.*, 2017, **399**, 506–514.
42 G. Li, W. Y. Yang, S. Gao, Q. Q. Shen, J. B. Xue, K. X. Chen and Q. Li, Creation of rich oxygen vacancies in bismuth molybdate nanosheets to boost the photocatalytic nitrogen fixation performance under visible light illumination, *Chem. Eng. J.*, 2021, **404**, 127115.
43 Z. Y. Liu, M. Luo, S. B. Yuan, L. H. Meng, W. M. Ding, S. D. Su, Y. Cao, Y. Y. Wang and X. M. Li, Boron-doped graphene quantum dot/bismuth molybdate composite photocatalysts for efficient photocatalytic nitrogen fixation reactions, *J. Colloid Interface Sci.*, 2023, **650**, 1301–1311.
44 L. Klag, A. Gaur, M. Stehle, S. Weber, T. L. Sheppard and J.-D. Grunwaldt, Role of Iron and Cobalt in 4-Component Bi–Mo–Co–Fe–O Catalysts for Selective Isobutene Oxidation Using Complementary Operando Techniques, *ACS Catal.*, 2023, **13**, 14241–14256.
45 J. J. Zhang, R. Q. Wei, D. Q. Yang, Y. Wang and B. B. Zhang, Searching for silicate nonlinear optical materials by combining calculation and experiment, *Inorg. Chem. Front.*, 2023, **10**, 4711–4718.
46 M. Luo, C. S. Lin, D. H. Lin and N. Ye, Rational Design of the Metal–Free $KBe_2BO_3F_2$·(KBBF) Family Member $C(NH_2)_3SO_3F$ with Ultraviolet Optical Nonlinearity, *Angew. Chem., Int. Ed.*, 2020, **59**, 15978–15981.
47 J. Heyd and G. E. Scuseria, Efficient hybrid density functional calculations in solids: assessment of the Heyd-Scuseria-Ernzerhof screened Coulomb hybrid functional, *J. Chem. Phys.*, 2004, **121**, 1187–1192.
48 J. W. Sun, R. C. Remsing, Y. B. Zhang, Z. R. Sun, A. Ruzsinszky, H. W. Peng, Z. H. Yang, A. Paul, U. Waghmare, X. F. Wu, M. L. Klein and J. P. Perdew, Accurate first-principles structures and energies of diversely bonded systems from an efficient density functional, *Nat. Chem.*, 2016, **8**, 831–836.
49 A. F. Van den Elzen and G. D. Rieck, Redetermination of the structure of Bi_2MoO_6, koechlinite, *Acta Crystallogr., Sect. B: Struct. Crystallogr. Cryst. Chem.*, 1973, **29**, 2436–2438.
50 V. I. Voronkova and V. K. Yanovskii, Polymorphism and Properties of Bi_2WO_6 and Bi_2MoO_6, *Phys. Status Solidi A*, 1986, **93**, 57–66.
51 P. S. Halasyamani, Asymmetric Cation Coordination in Oxide Materials: Influence of Lone-Pair Cations on the Intra-octahedral Distortion in d^0 Transition Metals, *Chem. Mater.*, 2004, **16**, 3586–3592.
52 T. Chen and G. S. Smith, The compounds and the phase diagram of MoO_3-Rich Bi_2O_3-MoO_3 system, *J. Solid State Chem.*, 1975, **13**, 288–297.
53 E. Vila, J. E. Iglesias, J. Galy and A. Castro, Synthesis and characterization of a novel bismuth–molybdenum oxide and study of its ionic conducting behavior, *Solid State Sci.*, 2005, **7**, 1369–1376.
54 M. R. Sun, C. X. Li, J. L. Shi, M.-H. Lee and J. Y. Yao, Defect diamond-like tellurides as infrared nonlinear optical materials with giant second-harmonic generation tensor, *Mater. Today Phys.*, 2023, **36**, 101166.
55 Z. X. Jiao, J. Quah, T. H. Syed, W. Wei, B. B. Zhang, F. Wang and J. Wang, Synthesis, crystal and electronic structures, linear and nonlinear optical properties, and photocurrent response of oxyhalides $CeHaVIO_4$ (Ha = Cl, Br; VI = Mo, W), *Dalton Trans.*, 2024, **53**, 2029–2038.
56 C. C. Jin, X. X. Jiang, C. Wu, K. Duanmu, Z. S. Lin, Z. P. Huang, M. G. Humphrey and C. Zhang, Giant Mid–Infrared Second–Harmonic Generation Response in a Densely–Stacked van der Waals Transition–Metal Oxychloride, *Angew. Chem., Int. Ed.*, 2023, **62**, e202310835.
57 V. Umapathy, A. Manikandan, S. Arul Antony, P. Ramu and P. Neeraja, Structure, morphology and opto-magnetic properties of Bi_2MoO_6 nano-photocatalyst synthesized by sol–gel method, *Trans. Nonferrous Met. Soc. China*, 2015, **25**, 3271–3278.
58 Z. J. Zhang, T. T. Zheng, J. Y. Xu, H. B. Zeng and N. Zhang, Carbon quantum dots/Bi_2MoO_6 composites with photocatalytic H^2 evolution and near infrared activity, *J. Photochem. Photobiol., A*, 2017, **346**, 24–31.
59 A. A. Savina, V. V. Atuchin, S. F. Solodovnikov, Z. A. Solodovnikova, A. S. Krylov, E. A. Maximovskiy, M. S. Molokeev, A. S. Oreshonkov, A. M. Pugachev and E. G. Khaikina, Synthesis, structural and spectroscopic properties of acentric triple molybdate $Cs_2NaBi(MoO_4)_3$, *J. Solid State Chem.*, 2015, **225**, 53–58.
60 X. L. Du, Z. L. Gao, F. A. Liu, X. J. Guo, X. M. Wang, Y. X. Sun and X. T. Tao, Anisotropic properties and Raman spectra of a $LiNa_5Mo_9O_{30}$ single crystal grown by the TSSG method, *CrystEngComm*, 2020, **22**, 7716–7722.
61 Z. X. Jiao, O. M. Mireles, K. Ensz, F. Wang, M. L. Liang, P. S. Halasyamani, B. B. Zhang, D. P. Rillema and J. Wang, Heteroanionic $LaBrVIO_4$ (VI = Mo, W): Excellence in Both Nonlinear Optical Properties and Photoluminescent Properties, *Chem. Mater.*, 2023, **35**, 6998–7010.
62 M. Wiegel and G. Blasse, Luminescence and nonlinear optical properties of bariumfluoromolybdate ($Ba_2MoO_3F_4$), *Solid State Commun.*, 1993, **86**, 239–241.
63 X. Y. Long, R. An, Y. Lv, X. Y. Wu and M. Mutailipu, $BaMo_3O_{10}$ Polymorphs with Tunable Symmetries and Properties, *Inorg. Chem.*, 2023, **62**, 10059–10063.
64 H. Jo, M. H. Lee and K. M. Ok, Order and Disorder: Toward the Thermodynamically Stable (-$BaMoO_2F_4$ from the Metastable Polymorph, *Chem. Mater.*, 2021, **33**, 1875–1882.
65 J. C. Hancock, M. L. Nisbet, W. G. Zhang, P. S. Halasyamani and K. R. Poeppelmeier, Periodic Tendril Perversion and Helices in the $AMoO_2F_3$ (A = K, Rb, NH_4, Tl) Family, *J. Am. Chem. Soc.*, 2020, **142**, 6375–6380.
66 P. A. Maggard, T. S. Nault, C. L. Stern and K. R. Poeppelmeier, Alignment of acentric $MoO_3F_3^{3-}$ anions in a polar material: $(Ag_3MoO_3F_3)(Ag_3MoO_4)Cl$, *J. Solid State Chem.*, 2003, **175**, 27–33.

67 M. Holland, M. D. Donakowski, E. A. Pozzi, A. M. Rasmussen, T. T. Tran, S. E. Pease-Dodson, P. S. Halasyamani, T. Seideman, R. P. Van Duyne and K. R. Poeppelmeier, Polar Alignment of Λ-Shaped Basic Building Units within Transition Metal Oxide Fluoride Materials, *Inorg. Chem.*, 2013, **53**, 221–228.

68 T. S. Spiridonova, S. F. Solodovnikov, A. A. Savina, Z. A. Solodovnikova, S. Y. Stefanovich, B. I. Lazoryak, I. V. Korolkov and E. G. Khaikina, Synthesis, crystal structures and properties of the new compounds $K_{7-x}Ag_{1+x}(XO_4)_4$ (X= Mo, W), *Acta Crystallogr., Sect. C: Struct. Chem.*, 2017, **73**, 1071–1077.